

Integration of GPS and InSAR Data for Resolving 3-Dimensional Crustal Deformation

Zheng-Kang Shen¹ and Zhen Liu²

¹Dept. of Earth, Planetary, and Space Sciences, University of California, Los Angeles

²California Institute of Technology

November 24, 2022

Abstract

We develop an algorithm to integrate GPS and InSAR data for a 3-dimensional crustal deformation field at the Earth's surface. In the algorithm discrete GPS data points are interpolated to obtain a 3-dimensional continuous velocity field, which is then combined with the InSAR line-of-sight (LOS) velocity data pixel by pixel using the least-squares method. Advantages of our method over previous ones are that: 1) The GPS data points are optimally interpolated by balancing a trade-off between spatial resolution and solution stability. 2) A new algorithm is developed to estimate realistic uncertainties for the interpolated GPS velocities, to be used as weights for GPS data in GPS-InSAR combination. 3) Realistic uncertainties for the InSAR LOS rate data are estimated and used as weights for InSAR data in GPS-InSAR combination. 4) The ramps and/or offsets of the InSAR data are globally estimated for all the images to minimize data misfit, particularly at regions where the data overlaps. Application of this method to real data from southern California shows its capability of successfully restoring 3-dimensional continuous deformation field from spatially limited GPS and dimensionally limited InSAR data. The deformation field reveals water withdrawal induced subsidence and drought caused uplift at various regions in southern California.

16 Abstract

17

18 We develop an algorithm to integrate GPS and InSAR data for a 3-dimensional crustal
19 deformation field at the Earth's surface. In the algorithm discrete GPS data points are
20 interpolated to obtain a 3-dimensional continuous velocity field, which is then combined with the
21 InSAR line-of-sight (LOS) velocity data pixel by pixel using the least-squares method.
22 Advantages of our method over previous ones are that: 1) The GPS data points are optimally
23 interpolated by balancing a trade-off between spatial resolution and solution stability. 2) A new
24 algorithm is developed to estimate realistic uncertainties for the interpolated GPS velocities, to
25 be used as weights for GPS data in GPS-InSAR combination. 3) Realistic uncertainties for the
26 InSAR LOS rate data are estimated and used as weights for InSAR data in GPS-InSAR
27 combination. 4) The ramps and/or offsets of the InSAR data are globally estimated for all the
28 images to minimize data misfit, particularly at regions where the data overlaps. Application of
29 this method to real data from southern California shows its capability of successfully restoring 3-
30 dimensional continuous deformation field from spatially limited GPS and dimensionally limited
31 InSAR data. The deformation field reveals water withdrawal induced subsidence and drought
32 caused uplift at various regions in southern California.

33

34 1. Introduction

35

36 The Global Positioning System (GPS) and the Interferometric Synthetic Aperture Radar (InSAR)
37 are two satellite geodesy methods that have been widely used in recent years to measure crustal
38 deformation. The GPS method can be used to precisely measure 3-dimensional positions and
39 displacements at discrete locations, with up to one millimeter accuracy in horizontal directions
40 and several millimeters accuracy in vertical direction (Bock and Melgar, 2016). The InSAR
41 techniques can be used to measure areal displacements in the direction of radar line-of-sight
42 (LOS) up to several millimeters to centimeter accuracy (Gens and Van Genderen, 1996). These
43 two methods are therefore complementary to each other for crustal deformation monitoring, and
44 efforts have been made to combine these two kinds of observations with common spatial and
45 temporal span, for better spatial and temporal resolution than using either one of them. Such
46 kinds of efforts include: 1) Construct a 3-dimensional velocity field using a GPS derived velocity
47 model to control the long-wavelength deformation and InSAR data to constrain the short-
48 wavelength deformation (e.g. Tong et al., 2013). 2) Interpolate 3-dimensional GPS velocity and
49 combine that with the InSAR LOS rate data by point-by-point least-squares regression (e.g.
50 Samsonov et al., 2007, 2008). 3) Integrate 3-dimensional GPS time series at discrete locations
51 with 1-dimensional InSAR LOS time series data for 3-dimensional continuous time series (e.g.
52 Gudmundsson et al., 2002). In this study we focus on the approach 2), and develop an algorithm
53 to optimally integrate GPS and InSAR data sets for the production of 3-dimensional crustal
54 velocity solution. We will also demonstrate the usefulness of the algorithm with a case study at a
55 selected region in southern California. This method can be extended further to the combination
56 of GPS and InSAR time series data. The code to perform the combination is released to
57 interested users as a supporting information dataset to this paper.

58

59 2. Methodology

60

61 2.1. GPS data interpolation and uncertainty estimation

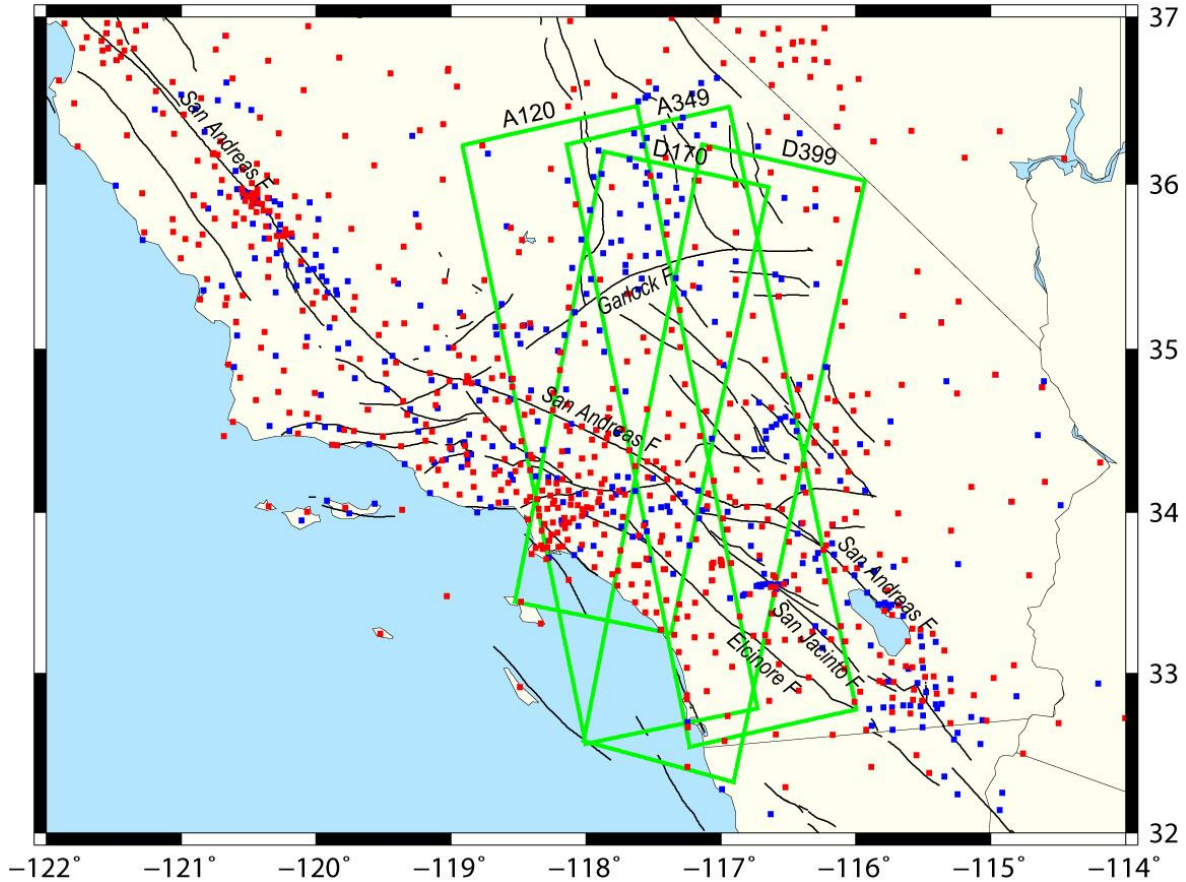


Figure 1. Study area in southern California. Black curves are active faults, red and blue squares are GPS sites whose 3D and 2D (horizontal only) data are used in this study respectively. The green frames denote the imprints of 4 InSAR tracks whose data are used in this study.

62 GPS station velocities can be derived from position time series of either campaign or continuous
 63 GPS observations. In this study as an example, we use velocity solutions of continuous GPS
 64 (CGPS) sites produced by the MEaSUREs project ([ftp://sopac-
 65 ftp.ucsd.edu/pub/timeseries/measures/ats/](ftp://sopac-ftp.ucsd.edu/pub/timeseries/measures/ats/)), and of campaign GPS sites from the SCEC Crustal
 66 Motion Map version 4 (CMM4) solution (Shen et al., 2011) (Figs. 1 and 2). The CMM4
 67 velocities are rotated to align with the CGPS solution which is referenced to the stable North
 68 America reference frame (SNARF) (Herring et al., 2008). We divide the GPS data into two
 69 groups. The first group utilizes the 3-dimensional velocity components for solution, which includes
 70 most of the CGPS sites from the MEaSUREs project. The second group utilizes only the
 71 horizontal velocity components, which includes the CMM4 sites and a small portion of the
 72 CGPS sites whose vertical velocities show anomalously large and possibly non-tectonic signals.
 73 Both data sets are screened to remove outliers, and 1052 horizontal and 542 vertical site
 74 velocities are employed. Separate interpolations are performed for the horizontal and vertical
 75 velocity fields, to account for different data populations.

76

77 In our algorithm of GPS and InSAR data integration, point-based discrete GPS velocities are first
 78 interpolated to produce continuous 3-D vector map at chosen grids. The interpolation is based on
 79 an algorithm of Shen et al. (2015), which takes into account GPS network density and
 80 configuration for data weighting. A Gaussian distance weighting function (w_d) and a Voronoi

81 cell spatial weighting function (w_v) are used in the interpolation, which allow greater weighting
 82 for sites located closer to the chosen grid and/or occupying greater Voronoi cell areal space. The
 83 amount of weighting and degree of smoothing can be spatially variable and optimally determined
 84 based on *in situ* data strength, and are realized by assigning a common weighting parameter W
 85 for all the grid points: $W = \sum_{i=1}^{n_k} w_d^i(k) * w_v^i(k)$. n_k is the number of neighboring data points
 86 used for the k^{th} grid point, $w_d^i(k) = \exp\left(-\frac{r_i^2}{\sigma_k^2}\right)$ is the Gaussian distance weighting function, r_i is
 87 the distance between the i -th GPS site and the grid point, and σ_k is the distance decay constant.
 88 At each grid point σ_k is adjusted to meet W , which is a predetermined constant. With this
 89 adjustment, less smoothing is performed and better resolution is achieved for grids with denser

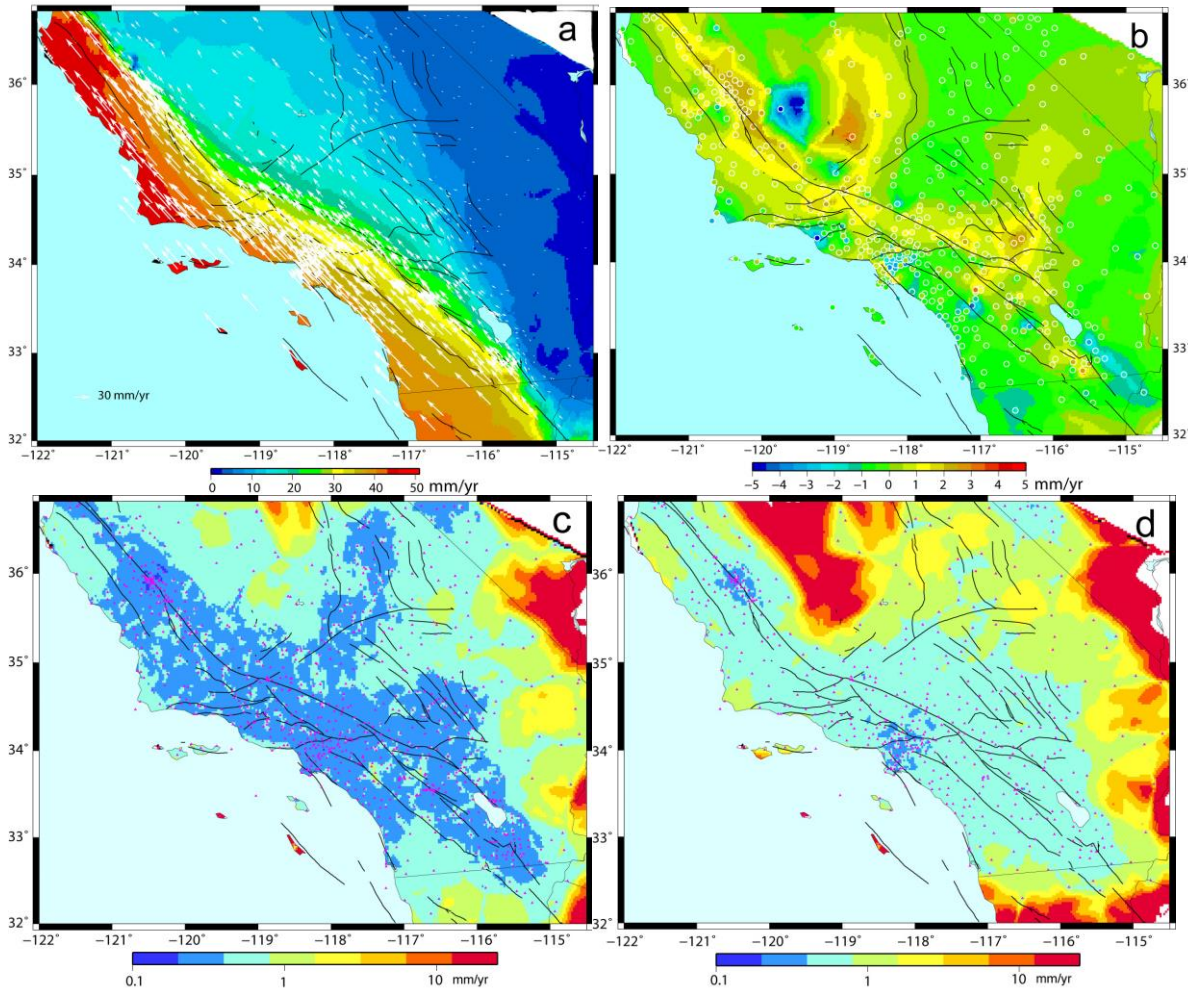


Figure 2. GPS velocities and interpretation result. (a) White vectors are GPS horizontal velocities in SNARF reference frame that are used in the combination with InSAR data. The background colors denote the amplitudes of interpolated horizontal velocity field. (b) Filled circles are GPS vertical observations, and the background colors denote the interpolated vertical velocity field. (c) and (d) are uncertainties of east and up components of interpolated GPS velocities, respectively. Magenta triangles denote the locations of GPS sites.

90 data coverage, and vice versa. This approach can also effectively smooth out the incoherencies in

91 discretized GPS velocity data and make robust joint inversion result. Selection of the parameter
 92 W allows an overall control of the degree of smoothing for the solution. Greater W would result
 93 in more sites included for interpolation and more smoothed solution with less resolution, and
 94 smaller W would result in less sites included and less smoothed solution with better resolution.
 95 An optimal balance can be achieved by assessing the overall data strength of the project.

96

97 To combine the interpolated GPS data with InSAR data, we need adequate estimates of GPS
 98 velocity uncertainties, to be used as data weighting in the combination. Formal GPS velocity
 99 uncertainties deduced in the interpolation process, however, are not fit for the job because they
 100 are largely determined by the amount of a priori information (i.e. the degree of smoothing)
 101 imposed during interpolation, which varies from grid to grid. It usually leads to apparently
 102 unreasonable results, that regions with sparser data points would have smaller uncertainty than
 103 regions with denser data points, and vice versa. To overcome the problem, we propose to
 104 propagate errors from GPS data input to interpolation output using the same interpolation
 105 functional form and least-square procedure as before, but not to alter the smoothing distance
 106 parameter σ_k . Instead, σ_k will be kept as a constant σ_0 for all the region, usually chosen as an
 107 average of previous σ_k in relatively denser network region. In this way the same kind of a priori
 108 assignment algorithm will be applied for all the grids, and the only difference reflected in the
 109 output uncertainty estimates will be the in situ data strength; the denser the local observation
 110 network is, the smaller the uncertainty will be, and vice versa. The overall weighting for GPS
 111 data is also rescaled proportionally by a constant factor applied to the solution uncertainties to
 112 satisfy: $\sum_i 1/\alpha_i^2 = \sum_i 1/\beta_i^2$, where α_i is the input horizontal or vertical velocity uncertainty for the
 113 i -th GPS site in the region, and β_i is the rescaled corresponding uncertainty for the interpolated
 114 velocity component at the site, respectively. The sum is over all the GPS sites in the study
 115 region. The only free parameter in the derivation is therefore σ_0 , which is set by the user and
 116 should be on the order of average spacing of the GPS station network.

117

118 2.2. InSAR data processing, LOS rate and uncertainty estimation

119

120 Here we briefly describe InSAR processing and analysis steps for the InSAR data used in the
 121 case study for southern California. We processed the raw SAR data of ERS-1,2 and Envisat
 122 satellites from 1992 to 2010 for interferograms using a modified version of JPL/Caltech
 123 ROI_PAC software package. Major processing steps include interferometric phase flattening
 124 using precise orbit, topography phase correction based on 2-arc SRTM digital elevation model
 125 (DEM), baseline re-estimation for orbital error correction when needed, phase unwrapping,
 126 filtering and geocoding. For the ERS-2 data after 2001 that have Doppler issue due to gyroscope
 127 failure, we employ a maximum entropy approach to resolve Doppler ambiguity and identify all
 128 usable ERS-2 interferometric pairs. For Envisat ASAR sensors, we correct temporally correlated
 129 range ramp error due to long-term local oscillator frequency drift by adopting an empirical
 130 approach (Marinkovic and Larsen, 2013). Comparison with in-situ GPS shows that such a
 131 correction works well and reduces the RMS error between InSAR and GPS velocities to less than
 132 2 mm/yr (Liu et al., 2014).

133

134 We use a variant of the Small Baseline Subset InSAR time series approach to solve for InSAR
 135 LOS time series and mean velocity (e.g., Sansosti et al., 2010). We incorporate topography
 136 dependent troposphere delay correction, residual DEM error and earthquake offset estimate, and
 137 employ spatiotemporal filtering to remove high frequency turbulent troposphere noise
 138 (Samsonov, 2010; Liu et al., 2014). Since orbital ramp error for data from the same track is
 139 typically limited to a few acquisitions (e.g., Fattahi & Amelung, 2014) and small, we correct
 140 only affected interferograms through baseline re-estimation with the constraint of a priori GPS

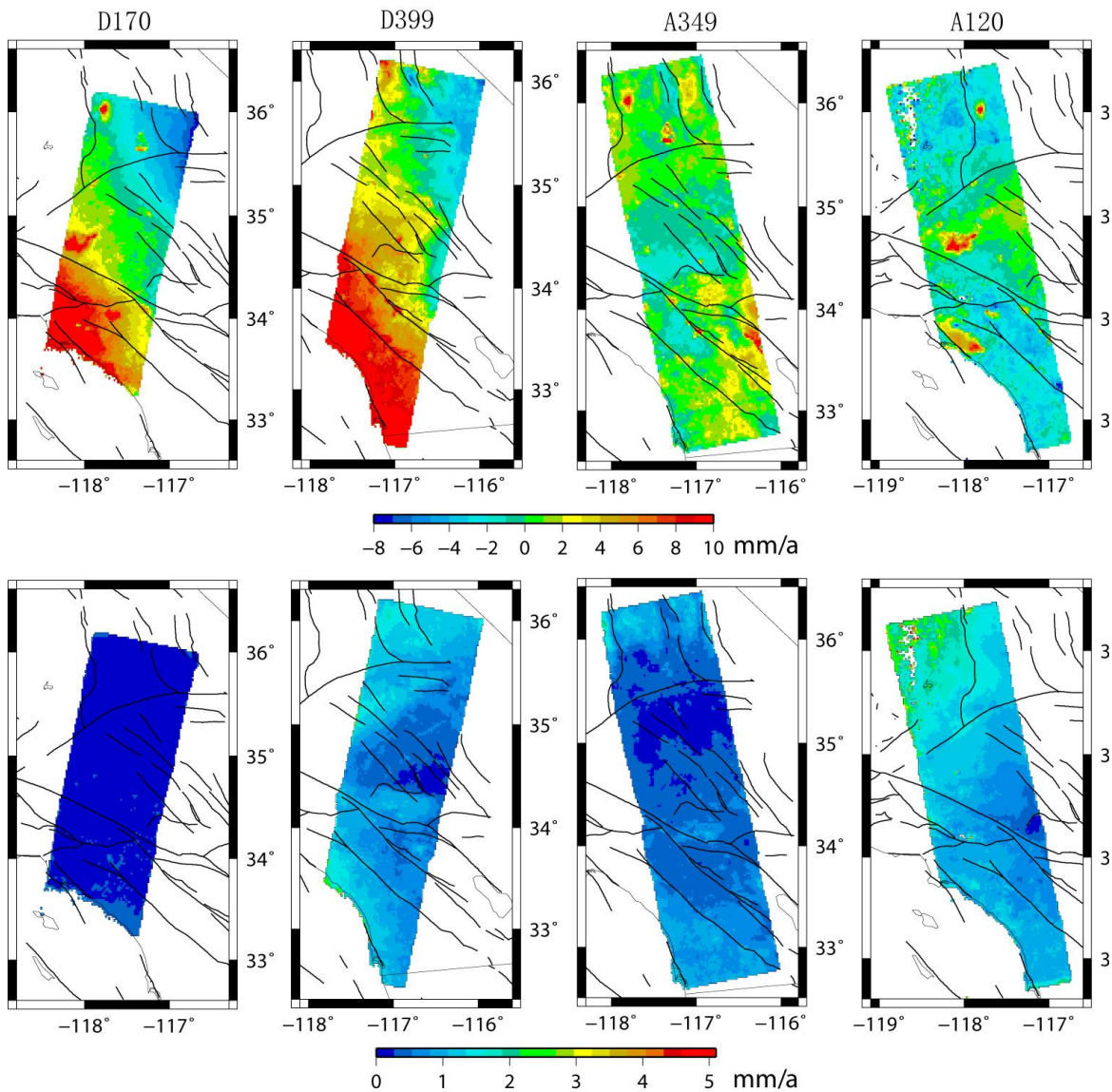


Figure 3. InSAR LOS data from 4 selected tracks of D170, D399, A349, and A120 that are used in the combination. The upper panel shows the LOS velocities, and the lower panel shows the corresponding uncertainties, respectively.

141 based deformation model. The number of pairs with such correction is much less than the total
 142 number of interferograms that went into the analysis. This ensures that the influence of a priori
 143 model is negligible. Hundreds of interferograms that meet spatial and temporal baseline criteria
 144 are formed and used in the time series inversion.

145 The InSAR data are weighted by their LOS uncertainties. To characterize the uncertainties
146 associated with InSAR deformation map, we adopt a Jackknife variance estimation approach
147 [Efron and Stein, 1981], which provides a reasonable way to account for uncertainties arisen
148 from lacking or missing dates, uncorrected residuals or other noises, and/or the influence of
149 reference pixel and date.

150

151 2.3. GPS and InSAR velocity data combination

152

153 We combine GPS interpolated velocities and InSAR LOS rate data to produce a spatially
154 continuous 3-dimensional velocity field. We first divide the region into rectangle grid cells. At
155 each grid cell, all of the available InSAR LOS rate data from different tracks (with different
156 viewing geometries) are used. For each of the LOS rate images all the pixel data within the grid
157 cell are averaged to produce a mean rate, weighted by the uncertainties. The binned averages are
158 also made for azimuth angle, look direction, and LOS uncertainty (which is averaged the same
159 way as the other observables) associated with the LOS measurements, and used as data inputs of
160 subsequent analysis.

161

162 Because of relative measurements and selections of different reference regions, the InSAR LOS
163 velocities usually have offsets between different tracks. The residual orbital error and/or
164 remaining atmospheric phase noise that are not fully corrected may also introduce some subtle
165 ramp difference between tracks. The first step in GPS/InSAR combination is to solve for the
166 offsets/ramps of InSAR images. Since InSAR data provide only LOS measurements from
167 ascending and/or descending viewing geometry, the offset/ramp parameters have to be solved
168 together with the 3-D deformation components, and some GPS data and their interpolated values
169 are therefore needed in the estimate to stabilize the inversion. Because these offset/ramp
170 parameters are correlated with all the deformation parameters in the study area, an optimal
171 estimate of the offsets/ramps means a global solution for all the parameters involved. However,
172 the number of parameters for the 3-D velocity field can be huge, up to millions or even billions
173 depending on the scope of the study area and the size of the grid cells provided, thus it may not
174 be practical and/or even necessary to solve for all the parameters in a single least-squares
175 solution. We therefore include GPS data at only a limited number of grid points in the solution in
176 this step. Two groups of grid points are accounted: the first group includes all the grid points
177 containing direct GPS velocity observations, and the second group involves decimated grid
178 points with multiple InSAR data entries. Incorporation of the data in the second category helps
179 reinforce the solution for the offsets/ramps, but only at decimated grid points (e.g. by a factor of
180 10 in each dimension in the overlapped regions) would be sufficient for the purpose.

181

182 In the second step the components of offsets/ramps are removed from the InSAR LOS data, and
183 the 3D velocity is solved for each grid cell through least-squares regression, with GPS
184 interpolated velocity and LOS data for the cell incorporated. The adaptive GPS and InSAR data
185 uncertainties are used to weight the data input. The GPS vertical data may or may not be used to
186 constrain the final solution, depending on the quality and reliability of the data.

187

188 3. GPS-InSAR combination in Southern California

189

190 3.1. GPS-InSAR data combination

191

192 We apply the GPS-InSAR combination method to a region in southern California covered by 4
 193 ground tracks of ERS and Envisat satellites (Fig. 1). The InSAR data delineate an area of
 194 approximately 32.5°-36°N, 116°-118.5°W, covering the southern part of the Eastern California
 195 Shear Zone, the Mojave Desert, the central Transverse Ranges, and the coastal area from Los
 196 Angeles to San Diego. Active faults in the region include the Mojave and San Bernardino
 197 segments of the San Andreas, Garlock, Mojave Shear Zone, Owens Valley, San Jacinto, and
 198 Elsinore faults.

199
 200 The GPS velocity dataset used in the study is shown in Fig. 2, along with the interpolated
 201 velocities and their uncertainties. As described in the previous section, we adopt an algorithm to
 202 determine uncertainties of the interpolated velocities, which employs the same degree of
 203 smoothing for all the grid cells, and considers GPS network distribution and site-specific
 204 uncertainties to determine uncertainties of the velocity solution. Here we set the data weighting
 205 threshold W for southern California to be 3, and the smoothing constant σ_0 for uncertainty
 206 evaluation to be 20 km. These parameters are determined after some trial-and-error, in
 207 accordance with the network spatial density in southern California. We also assign the lower
 208 thresholds of uncertainties for horizontal and vertical GPS velocity data input as 0.5 mm/yr and
 209 1.0 mm/yr respectively, considering epistemic errors of the CGPS site velocity estimates. The
 210 final solution does not seem to be sensitive to the changes of these values within the same order
 211 of magnitude.

212
 213 Four tracks of InSAR data sets are used in the study (Fig. 3). The data are the LOS velocities
 214 from our previous InSAR time series analysis (Liu et al., 2014), including the following: (a)
 215 descending track 170 derived from ERS/Envisat data over the period of 1992-2010; (b)
 216 descending track 399 from Envisat over the period of 2003-2010; (c) ascending track 349 from
 217 Envisat over the period of 2003-2010; and (d) ascending track 120 from Envisat over the period
 218 of 2003-2010. The lower panel of Fig. 3 shows the estimated uncertainties for the LOS velocity
 219 data, which shows that although uncertainties are relatively uniform for track 170, they vary
 220 considerably for tracks 399, 349, and 120. For tracks 399, 349, and 120, we only use Envisat
 221 data for interseismic velocity estimates as these tracks spanning the East California Shear Zone
 222 (ECSZ). The ERS data from these tracks are not used because they are likely affected by
 223 postseismic deformation following the 1992 Landers and 1999 Hector Mines earthquakes in the
 224 ECSZ area. This is resulted in fewer SAR images for tracks 399, 349, and 120 than for track 170,
 225 and among which a few images were affected significantly by atmospheric disturbance with
 226 strong spatial variations. This is particularly true for track 120, with the residual atmosphere
 227 noise resulting in the largest errors for the northern part of the track where the LOS rate
 228 uncertainties are up to 4 mm/yr.

229
 230 A suite of combination models are tested with various selection of model parameters, including
 231 the choices of InSAR data uncertainties, the use of GPS vertical data for model constraints, and
 232 the InSAR offset/ramp estimation, etc. Table 1 lists parameter setups of six models tested and the
 233 modeling statistics.

234

235 **Table 1.** Combination model results.

236 Model #	InSAR- σ	GPS Vertical	Ramp/Offset	χ_w^2	χ_w^2/n	χ_{uw}^2	χ_{uw}^2/n
-------------	-----------------	--------------	-------------	------------	--------------	---------------	-----------------

237	A	Estimated	Not used	Ramp	30479	0.76	35393	0.88
238	B	Default	Not used	Ramp	9090	0.23	36360	0.91
239	C	Estimated	Used	Ramp	52783	1.32	62138	1.55
240	D	Default	Used	Ramp	20500	0.51	81999	2.05
241	E	Estimated	Not used	Offset	55032	1.37	64130	1.60
242	F	Default	Not used	Offset	16403	0.41	65612	1.64

243 χ_w^2 : Total weighted postfit residual χ^2 .
 244 χ_w^2/n : Reduced weighted postfit residual χ^2 .
 245 χ_{uw}^2 : Total unweighted postfit residual χ^2 .
 246 χ_{uw}^2/n : Reduced unweighted postfit residual χ^2 .

247
 248 Fig. 4 shows the result of model A, which has 3 common parameters solved for each InSAR

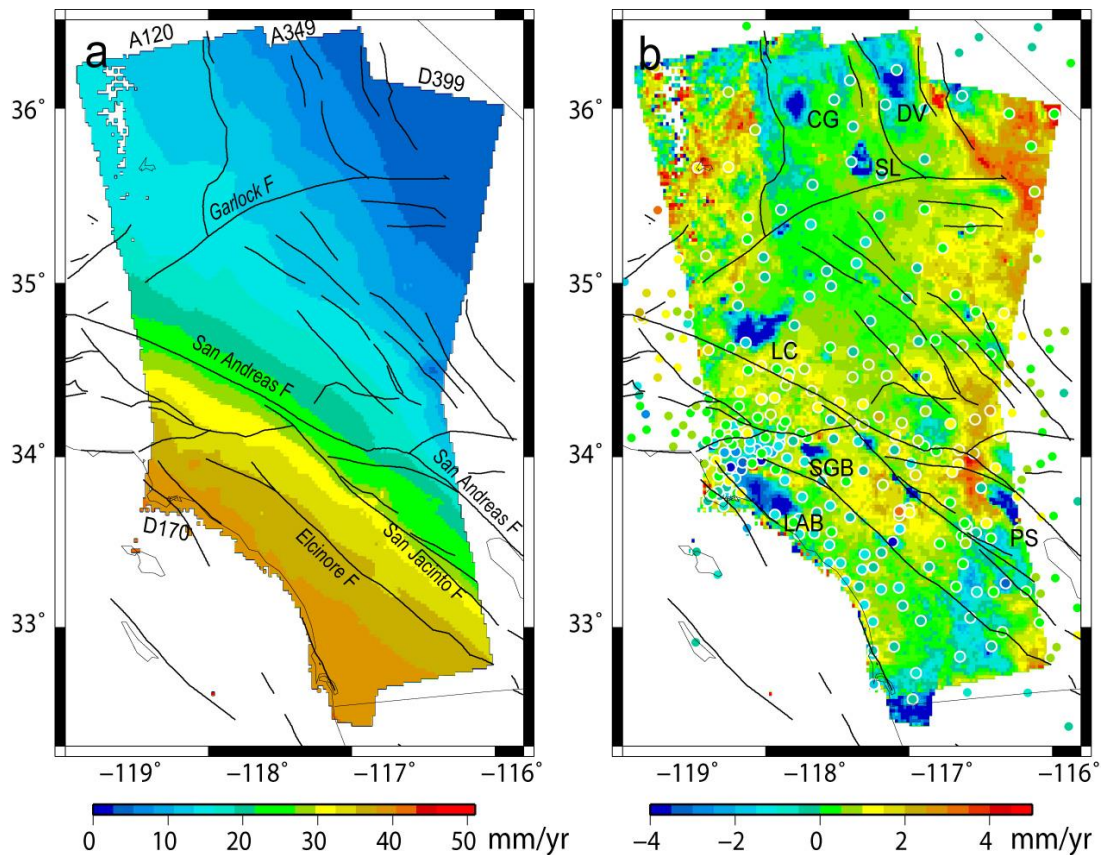


Figure 4. Combined GPS and InSAR 3-D velocities for Model A, with estimated InSAR data uncertainties to weight the data and SAR satellite orbital ramps estimated. (a) shows amplitudes of the horizontal components, and (b) the vertical components, respectively. Round dots in (b) are GPS vertical velocities, which are used in the orbital ramps estimation but not the 3-D velocity solution. Name abbreviations: CG, Coso Geotherm site; DV, Death Valley; LAB, Los Angeles Basin; LC, Lancaster; PS, Palm Springs; SB, San Gabriel Basin; SL, Searles Lake.

249 image, namely the constant offset and the east and north trends for the ramp. The estimated LOS
 250 uncertainties are used to weight the data, with a lower cut-off threshold of 1 mm/yr. This ad hoc
 251 cut-off threshold is set to account for the effects of residual atmospheric noise or other
 252 unmodeled noise. The GPS vertical data are used in derivation of the ramps of the InSAR data
 253 but not the final solution of the vertical velocities. The InSAR data postfit residuals and the

254 model formal uncertainties are demonstrated in Fig. 5. Only the uncertainties of the east and
 255 vertical components are shown. Uncertainties of the north component are not shown which are
 256 very similar to that of the east component.

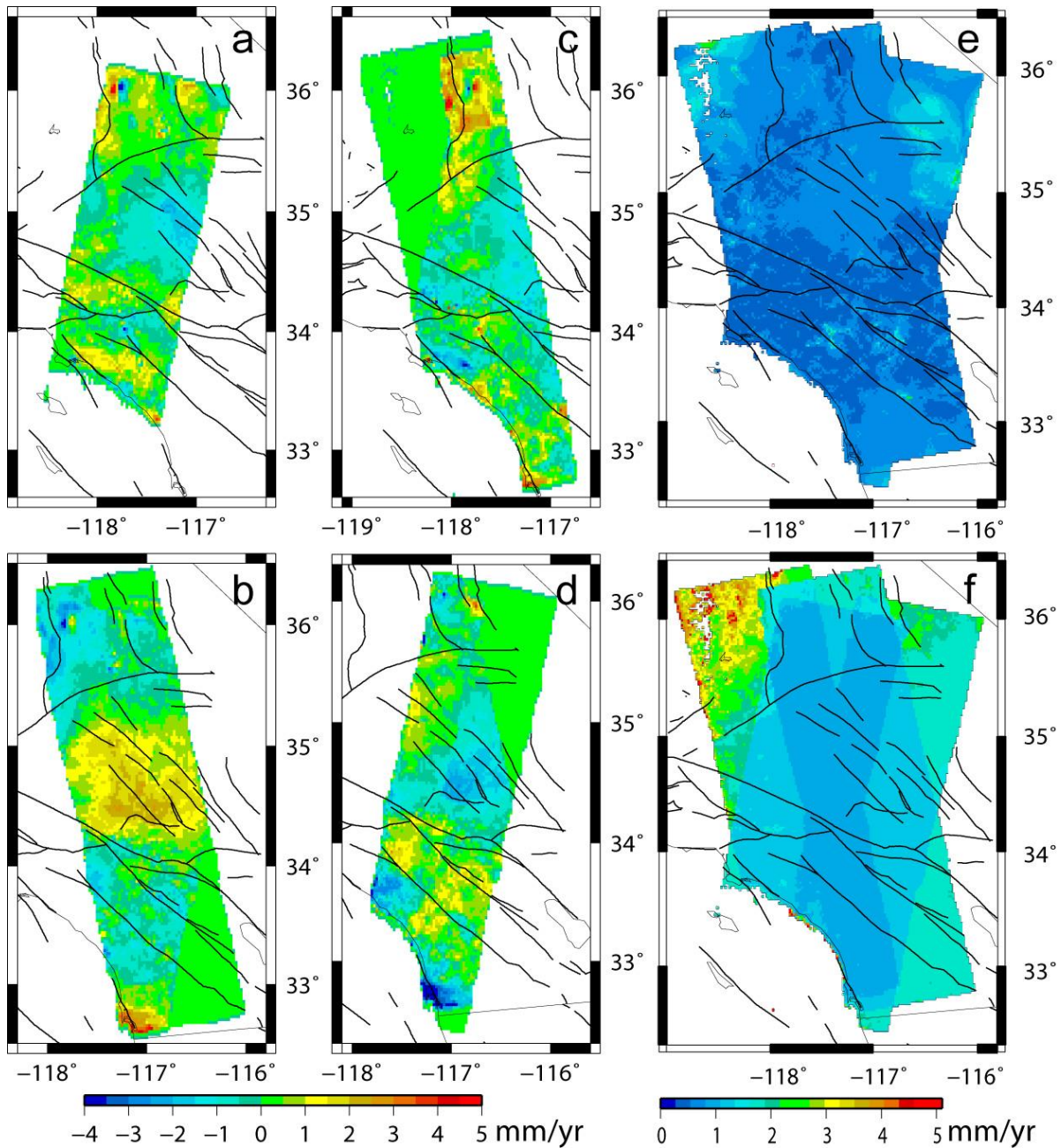


Figure 5. Data postfit residuals and solution uncertainties for Model A. (a), (b), (c), and (d) are InSAR LOS postfit residuals for tracks D170, A349, A120, and D399, respectively. (e) and (f) are solution uncertainties for the east and vertical components respectively.

257 Fig. 6 shows the 3-D velocity solution for Model B, which is similar to Model A except that
 258 instead of estimated uncertainties for InSAR data, a default LOS uncertainty of 2 mm/yr is
 259 adopted to constrain the solution. The InSAR data postfit residuals and the model formal
 260 uncertainties are demonstrated in Fig. S1.

261 |

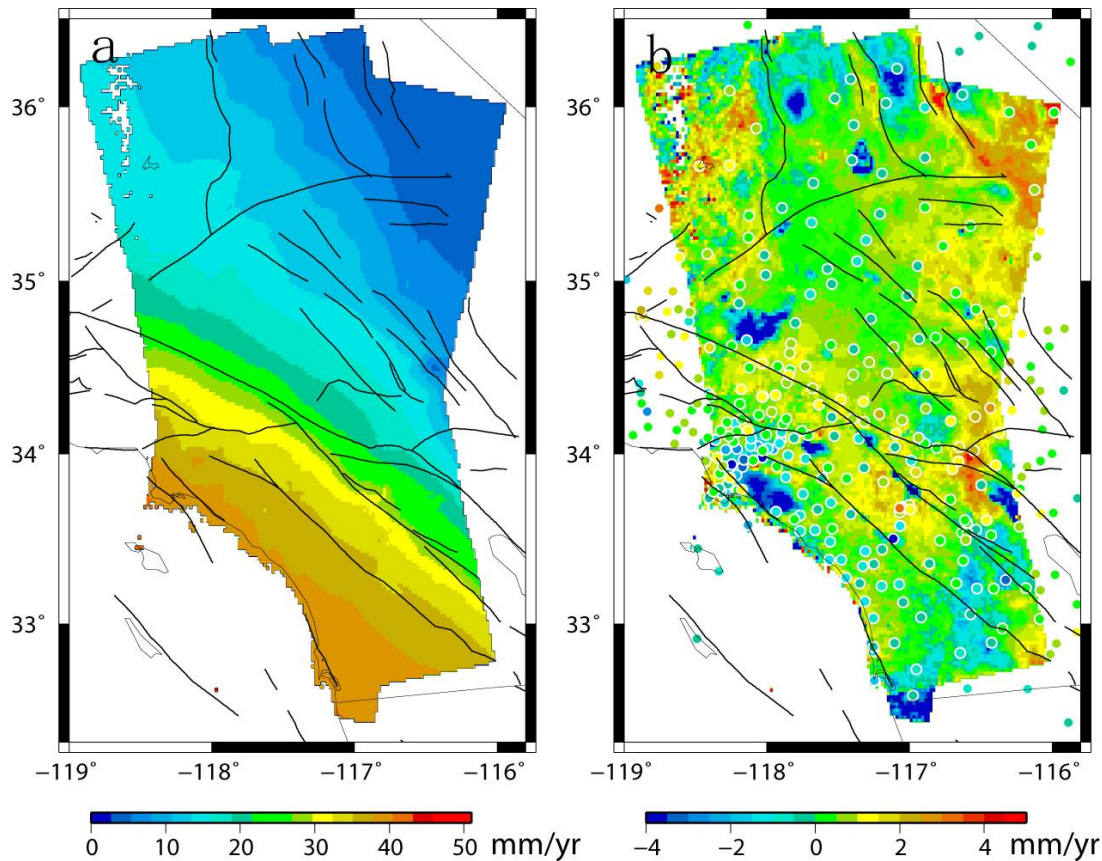


Figure 6. Combined GPS and InSAR 3-D velocities for Model B, with default InSAR data uncertainties (2 mm/yr) to weight the data and SAR satellite orbital ramps estimated. (a) shows amplitudes of the horizontal components, and (b) the vertical components, respectively. Round dots in (b) are GPS vertical velocities, which are used in orbital ramps estimation but not the 3-D velocity solution.

262 Four other solutions for Models C, D, E, and F are shown in Figs. 7, S3, S5, and S7, whose
 263 parameterizations are defined in Table 1. Figs. S2, S4, S6, and S8 plot the InSAR data postfit
 264 residuals and the solution uncertainties for the four models respectively.

265

266 3.2. Result discussion

267

268 In this study we explored six models of GPS-InSAR data combination with different options of
 269 model constraints, such as (a) whether to estimate the ramps of satellite orbits, (b) whether to use
 270 default of estimated uncertainties to condition the InSAR data, and (c) whether to use GPS
 271 vertical velocities to constrain the final solution of vertical velocity field. Comparing all the
 272 solutions, we find that the GPS-InSAR combined horizontal velocity fields of the six models are
 273 very similar to the GPS interpolated horizontal velocity field, and the differences are at the sub-
 274 millimeter per year level for all the data points. The results suggest that the horizontal velocity
 275 solution is mostly resolved by the GPS data, and contribution from the InSAR data is relatively
 276 minor. Consistency of all the model results also suggests that InSAR and GPS observations are
 277 in good agreement in documenting the horizontal deformation field, with both velocity solutions
 278 deduced using data of overlapped time span of 6-20 years.

279
 280
 281
 282
 283
 284
 285
 286
 287
 288
 289
 290
 291
 292
 293
 294

The difference in model constraints and/or parameterization, however, can have significant impact on vertical velocity solution and its error assessment. One of the factors involved in the combination is whether to use the GPS vertical data to constrain the pixel solution. Figs. 4 and 7 show the velocity solutions of Models A and C, for which all the parameterizations are the same except that Model C incorporated GPS vertical data to constrain the model and Model A did not. Comparison of the two solutions reveals that, although inclusion of the GPS vertical data has provided additional constraints to the solution, its lack of detailed spatial resolution smeared and missed some regional deformation signals. For example, up to 8 mm/a subsidence is shown in the Lancaster, Los Angeles basin, and San Gabriel basin regions in the solutions without using GPS vertical data as constraints (Model A, Fig. 4), which are however absent or significantly suppressed in the solutions using GPS vertical data constraints (Model C, Fig. 7). These signals, detected by InSAR observations are caused by ground water withdrawal and shallow aquifer compaction (e.g., Galloway et al., 1998; Hoffmann et al., 2003) and are real, but cannot be picked up by GPS due to limited network spatial coverage (or missed time window).

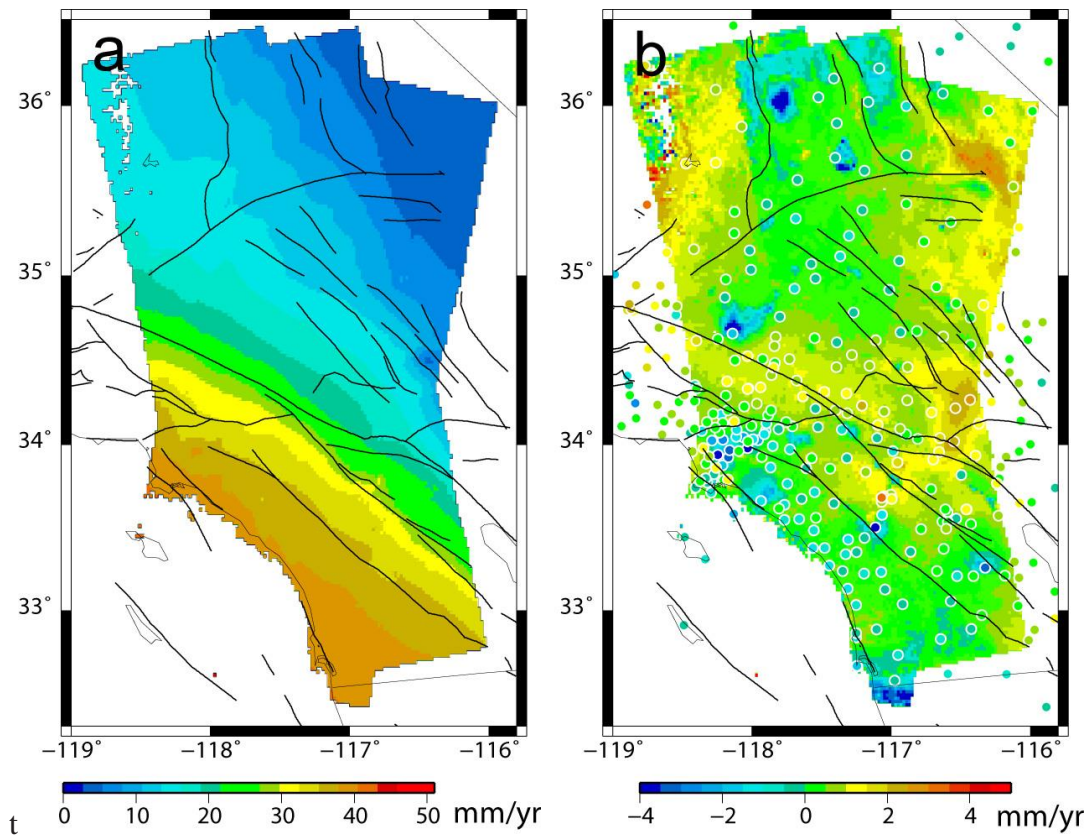


Figure 7. Combined GPS and InSAR 3-D velocities for Model C, with estimated InSAR data uncertainties to weight the data and SAR satellite orbital ramps estimated. (a) shows amplitudes of the horizontal components, and (b) the vertical components, respectively. Round dots in (b) are GPS vertical velocities, which are used in both estimation of orbital ramps and the final 3-D velocity solution.

295 The GPS data, on the other hand, provide effective constraints for mid to long range vertical
 296 deformation (>100 km in scale), associated with earthquake cycle and tectonic deformation. This
 297 is evidenced by the vertical deformation pattern shown in Fig. 4, which is similar to that reported

298 by Howell et al. (2016). We therefore use GPS vertical data to correct for the offsets/ramps of
299 the InSAR data and to stabilize the long range deformation, but not to use that to constrain the
300 local deformation.

301
302 Two sets of InSAR LOS data errors are adopted to constrain the solution in this study. One set of
303 solutions assumes a uniform data error of 2 mm/a (Models B, D, and F), which is a common
304 practice when no detailed error analysis is available. Another set of solutions takes the estimated
305 uncertainties derived using the Jackknife variance estimation approach (Models A, C, and E).
306 Using the estimated uncertainties to weight the InSAR data, the result shows no noticeable
307 difference from the one assuming uniform InSAR data uncertainty (e.g. Fig. 4 vs. Fig. 6).
308 However, solution uncertainties hence derived for the two kinds of models are quite different.
309 The models assuming uniform LOS rate error deduce the uncertainty estimates with a spatial
310 pattern dictated mostly by InSAR data coverage, i.e. the redundancy distribution of the
311 observations (e.g. Fig. S1f). The models using the estimated LOS rate error yield the uncertainty
312 estimates taking into account of the InSAR data quality and observation history, reflecting better
313 the true data strength and weakness. For example, the solution uncertainty estimates shown in
314 Fig. 5f illuminates not only the impact of spatial pattern of InSAR data redundancy, but also the
315 relative strength of the data input, such as the largest uncertainties (up to 4 mm/yr) in the
316 northwest corner of the studied region, resulted from weak data entry of track 120.

317
318 We test different ways to remove the orbital effect from the InSAR data, and examine how that
319 affect the data fitting of the model. Two model parameterizations are tested, one is to solve for
320 an offset (i.e. Models E and F), and another is to solve for a ramp and an offset (i.e. Models A
321 and B) for each of the InSAR data images respectively. The results show that by adding two free
322 parameters for each track of the InSAR data, the orbital ramp model is able to reduce the data
323 postfit residual chisquares by half with respect to the orbital offset model (see statistics in Table
324 1), attesting the necessity of ramp correction in a joint inversion involving multiple InSAR data
325 entries. Significant jumps can also be seen for vertical solutions across some of the InSAR data
326 boundaries for the models adopted offset correction only (Figs. S5 and S7), which however are
327 much reduced for the vertical solutions of the models adopted ramp corrections (Figs. 4 and 6).
328 And for the data postfit residual plots, the ones for the offset removal model show significant
329 jumps at the edges of image overlaps (Figs. S6 and S8), which however are much suppressed for
330 the ones in the ramp removal model (Figs. 5 and S1).

331
332 3.3. Result interpretations

333
334 Based on the above discussion, we think that Model A takes the most optimal approach, and its
335 result is therefore the basis for our following interpretation (Fig. 4).

336
337 For the region in southern California under investigation, the horizontal velocity solution is
338 mostly determined by GPS data, with the formal uncertainties below 0.7 mm/yr for most of the
339 area (Fig. 5). The highest velocity gradient appears across the San Andreas and San Jacinto fault
340 system, consistent with previous findings about the deformation pattern in southern California
341 (e.g. Feigl et al., 1993; McCaffrey, 2005; Zeng and Shen, 2017). The formal uncertainties for the
342 vertical component are mostly determined by InSAR data, with < 1.5 mm/yr uncertainties for
343 most of the region with more than one LOS data entry, and < 2.5 mm/yr for most of the regions

344 with only one LOS data entry (Fig. 5). One significant exception is for the region near southeast
345 Central Valley at the northwest corner of the study region, where the formal uncertainties are up
346 to 4.5 mm/yr. This is due to relatively short duration and fewer observations for the A120 track
347 of InSAR data. Close to zero residuals usually appear at edges of the study region, where only
348 data from a single InSAR LOS image are available, and the solution uncertainties are relatively
349 larger.

350

351 Local subsidence is found at several locations in southern California, such as the Los Angeles
352 basin, Lancaster area in western Mojave, Coso geotherm site, Searles Lake, San Gabriel basin,
353 Death Valley, Palm Springs, and area spanning the southern sections of the San Jacinto and
354 Elsinore faults (Fig. 4). The subsidence ranges 3-8 mm/yr, and possibly caused by the loss of
355 ground water or contraction of geothermal/volcanic activity. Most of these subsidence features
356 are recorded by more than one SAR images, and reliable. About 1-2 mm/yr subsidence appears
357 across the southern plate boundary fault system including the San Andreas, San Jacinto, and
358 Elsinore faults, which is slightly higher than most of the GPS observed vertical velocities. The
359 result is mainly derived from the southeast edge of the image of track A349, and suffers from
360 relatively larger uncertainties (~1.8 mm/yr, Fig. 5f). More SAR data coverage in the region is
361 needed to further confirm the feature of deformation.

362

363 Scattered uplift of about 1-3 mm/yr appears in southern Great Valley, and may be due to
364 hydrologic effect associated with drought and crust rebound of the region (Fig. 4). The solution
365 uncertainties however are ~2-3 mm/yr and impede further interpretations. Uplift of about 1-3
366 mm/yr is also found from northern San Jacinto Mountains across the Banning and Northern San
367 Andreas faults to southern Mojave Desert. The result is in general consistent with the GPS
368 vertical measurements and seems to be credible, with the solution uncertainties less than 1
369 mm/yr (Fig. 2). The area around the east end of the Garlock fault shows 2-4 mm/yr uplift, which
370 however is not consistent with the GPS vertical velocities in the region. This deformation pattern
371 is solved with InSAR data from the descending track 399 only, with the solution uncertainties of
372 ~2 mm/yr. Input of more InSAR data from this area will help resolve deformation pattern of the
373 region.

374

375 **4. Conclusions**

376

377 We devise an algorithm to optimally combine GPS and InSAR data and produce 3-dimensional
378 velocity field at Earth's surface. At the locations where both InSAR and interpolated GPS data
379 are available, optimal 3-dimensional velocity components are derived using a weighted least-
380 square method. Both GPS and InSAR data uncertainties are used to weight the observables in
381 joint inversion. A GPS-InSAR combination code is provided for public use. This algorithm is
382 applied to modeling deformation field at a selected region in southern California. Conclusions
383 are the following.

- 384 1. Using optimally estimated GPS and InSAR uncertainties to weight the data provides proper
385 accounting of the solution uncertainties, and helps adequately assess the solution quality and
386 reliability.
- 387 2. Including InSAR data from both ascending and descending viewing geometry, if available,
388 provides improved constraint on the 3-D deformation when integrating with GPS data.
- 389 3. The approach of using GPS vertical data to constrain deformation field should be subject to

390 evaluation of data quality and deformation pattern. In southern California, the current GPS
 391 network is still too sparse to adequately detect localized vertical deformation, particularly in
 392 regions affected by hydrologic processes. Existence of certain outliers in the dataset makes
 393 identification of localized deformation even more challenging. The optimal approach is
 394 therefore to use the GPS vertical data to constrain the satellite orbital ramps only, and leave
 395 the localized vertical deformation solved by InSAR, aided by GPS horizontal constraints.

396 4. The GPS and InSAR data are generally consistent for the horizontal velocities at sub-
 397 millimeter per year level. The vertical velocity field is determined much better of the
 398 combined solution than using GPS data only, especially for regions experiencing localized
 399 deformation. These regions include the Los Angeles basin, San Gabriel basin, Lancaster,
 400 Palm Springs, Searles Lake, and Death Valley where hydrologic processes caused induced
 401 subsidence of up to 3-8 mm/yr. They also include the southern Great Valley region which
 402 underwent drought related uplift of 2-3 mm/yr. Uplift of 1-3 mm/yr is detected across a
 403 transect from the northern San Jacinto Mountains to southern Mojave Desert.

404 **Acknowledgments**

405 We thank ESA for open policy for ERS and Envisat data and UNAVCO for archiving the data
 406 and orbital products (www.unavco.org). Continuous GPS displacement time series and velocity
 407 were produced by JPL and SIO's Orbit and Permanent Array Center (SOPAC) with support from
 408 NASA MEaSUREs program and available from MEaSUREs project ([ftp://sopac-
 409 ftp.ucsd.edu/pub/timeseries/measures/ats/WesternNorthAmerica/](ftp://sopac-ftp.ucsd.edu/pub/timeseries/measures/ats/WesternNorthAmerica/)). Part of the research was
 410 performed under a contract with the National Aeronautics and Space Administration at the Jet
 411 Propulsion Laboratory, California Institute of Technology. This research was supported by the
 412 Southern California Earthquake Center (Contribution No. 9994). SCEC is funded by NSF
 413 cooperative Agreement EAR-1600087 and USGS Cooperative Agreement G12AC20047.

414

415 **Data Statement**

416 This supporting information file supplement to this submission includes figures which demonstrate
 417 combined 3D velocity solutions for models D and E, and the InSAR data postfit residuals for models B,
 418 C, D, E, and F. The supporting information dataset files submitted separately to and can be accessed
 419 through the Harvard Dataverse website <https://doi.org/10.7910/DVN/OQFSQB>. The file includes a sample
 420 run of the software to combine the GPS and InSAR data for a 3-D velocity solution. The GPS velocity
 421 data are from a combination of the solutions from the continuous GPS network from the MEaSUREs
 422 project (<ftp://sopac-ftp.ucsd.edu/pub/timeseries/measures/ats/WesternNorthAmerica/>) and the campaign GPS
 423 network from the CMM4 project (Shen et al., 2011). The InSAR data are the LOS rate estimates of 4
 424 tracks of ERS/Envisat measurements, averaged at 0.02 x 0.02 degree grids. The solution is for model A,
 425 with the following parameterization: (a) the estimated LOS rate data uncertainties are used for InSAR
 426 data weighting, (b) both the offsets and ramps are estimated for SAR satellite orbital errors, and (c) the
 427 GPS vertical data are not used to constrain the final pixel by pixel solution.

428 **References**

429 Bock, Y., & Melgar, D. (2016), Physical applications of GPS geodesy: a review. *Reports on*
 430 *Progress in Physics*, 79(10), 106801.

- 431 Efron, B., and Stein, C. (1981), The Jackknife Estimate of Variance, *The Annals of Statistics*,
 432 9(3): 586–596. doi:10.1214/aos/1176345462.
- 433 Fattahi, H. and F. Amelung (2014), InSAR uncertainty due to orbital errors, *Geophy J. Int*,
 434 199(1), 549-560, doi: 10.1093/gji/ggu276.
- 435 Galloway, D. L., Hudnut, K. W., Ingebritsen, S. E., Phillips, S. P., Peltzer, G., Rogez, F., &
 436 Rosen, P. A. (1998), Detection of aquifer system compaction and land subsidence using
 437 interferometric synthetic aperture radar, Antelope Valley, Mojave Desert, California. *Water*
 438 *Resources Research*, 34(10), 2573-2585.
- 439 Gens, R., & Van Genderen, J. L. (1996), Review Article SAR interferometry—issues,
 440 techniques, applications. *International Journal of Remote Sensing*, 17(10), 1803-1835.
- 441 Gudmundsson, S., F. Sigmundsson, and J. M. Carstensen (2002), Three-dimensional surface
 442 motion maps estimated from combined interferometric synthetic aperture radar and GPS
 443 data, *J. Geophys. Res.*, 107(B10), 2250, doi:10.1029/2001JB000283.
- 444 Herring, T., Craymer, M., Sella, G., Snay, R., Blewitt, G., Argus, et al. (2008, May), SNARF
 445 2.0: a regional reference frame for North America. In *AGU Spring Meeting Abstracts*.
- 446 Hoffmann, J., Galloway, D. L., & Zebker, H. A. (2003), Inverse modeling of interbed storage
 447 parameters using land subsidence observations, Antelope Valley, California. *Water*
 448 *Resources Research*, 39(2).
- 449 Howell, S., Smith-Konter, B., Frazer, N., Tong, X., & Sandwell, D. (2016), The vertical
 450 fingerprint of earthquake cycle loading in southern California. *Nature Geoscience*, 9(8),
 451 611-614.
- 452 Liu, Z., P. Lundgren, Z. Shen (2014), Improved imaging of Southern California crustal
 453 deformation using InSAR and GPS, *SCEC Annual Meeting*, SCEC contribution# 2038.
- 454 Marinkovic, P., Larsen, Y. (2013), Consequences of Long-Term ASAR Local Oscillator
 455 Frequency Decay - an Empirical Study of 10 Years of Data, *ESA Living Planet Symposium*,
 456 Edinburgh, UK.
- 457 Samsonov, S., Tiampo, K., Rundle, J., & Li, Z. (2007), Application of DInSAR-GPS
 458 optimization for derivation of fine-scale surface motion maps of Southern California. *IEEE*
 459 *Transactions on Geoscience and Remote Sensing*, 45(2), 512-521.
- 460 Samsonov, S. V., Tiampo, K. F., & Rundle, J. B. (2008), Application of DInSAR-GPS
 461 optimization for derivation of three-dimensional surface motion of the southern California
 462 region along the San Andreas fault. *Computers & Geosciences*, 34(5), 503-514.
- 463 Samsonov, S. (2010), Topographic correction for ALOS PALSAR Interferometry, *IEEE*
 464 *Transactions on Geoscience and Remote Sensing*, 48(7), 3020-3027.
- 465 Sansosti, E., F. Casu, M. Manzo, R. Lanari (2010), Space-borne radar interferometry techniques
 466 for the generation of deformation time series: An advanced tool for Earth's surface
 467 displacement analysis, *Geophys. Res. Lett.*, v. 37, L20305, doi:10.1029/2010GL044379.
- 468 Shen, Z.-K., R. King, D. Agnew, et al. (2011), A unified analysis of crustal motion in Southern
 469 California, 1970-2004: The SCEC Crustal Motion Map, *J. Geophys. Res.*, 116, B11402,
 470 doi:10.1029/2011JB008549.
- 471 Shen, Z. K., M. Wang, Y. Zeng, and F. Wang (2015), Strain determination using spatially
 472 discrete geodetic data, *Bull. Seismol. Soc. Am.*, 105(4), 2117–2127, doi:
 473 10.1785/0120140247.
- 474 Tong, X., D. T. Sandwell, and B. R. Smith-Konter (2013), High-resolution interseismic velocity
 475 data along the San Andreas Fault from GPS and InSAR, *J. Geophys. Res.-Solid Earth*, 118,
 476 369–389, doi:10.1029/2012JB009442.
- 477